A Factor-Image Framework to Quantification of Brain Receptor Dynamic PET Studies

Z. Jane Wang, *Member, IEEE*, Zsolt Szabo, Peng Lei, József Varga, and K. J. Ray Liu, *Fellow, IEEE*

***Abstract*—The positron emission tomography (PET) imaging technique enables the measurement of receptor distribution or neurotransmitter release in the living brain and the changes of the distribution with time and thus allows quantification of binding sites as well as the affinity of a radioligand. However, quantification of receptor binding studies obtained with PET is complicated by tissue heterogeneity in the sampling image elements (i.e., voxels, pixels). This effect is caused by a limited spatial resolution of the PET scanner. Spatial heterogeneity is often essential in understanding the underlying receptor binding process. Tracer kinetic modeling also often requires an intrusive collection of arterial blood samples. In this paper, we propose a likelihood-based framework in the voxel domain for quantitative imaging with or without the blood sampling of the input function. Radioligand kinetic parameters are estimated together with the input function. The parameters are initialized by a subspace-based algorithm and further refined by an iterative likelihood-based estimation procedure. The performance of the proposed scheme is examined by simulations. The results show that the proposed scheme provides reliable estimation of factor time-activity curves (TACs) and the underlying parametric images. A good match is noted between the result of the proposed approach and that of the Logan plot. Real brain PET data are also examined, and good performance is observed in determining the TACs and the underlying factor images.**

***Index Terms*—Brain receptor study, compartmental model, distribution volume, dynamic imaging, likelihood, PET, tracer kinetic modeling, voxel-domain quantitative imaging.**

I. Introduction

FUNCTIONAL imaging techniques, such as positron emission tomography (PET), single photon emission computed tomography (SPECT), and magnetic resonance imaging (MRI), represent powerful tools for the visualization and elucidation of important molecular mechanisms [1], while high-resolution MRI supplies the structural details that PET and SPECT may lack. The fundamental aim of functional imaging is to extract quantitative information about physiological function (e.g., physiological parameters) from medical images. For example, using PET and a specific radioligand, the serotonin transporter (SERT) in the brain can be quantified to assess the integrity of serotonergic neurotransmission [2]. PET is a nuclear imaging technique relying on the unique physics of radionuclide that decay via positron emission. More recently, PET imaging has found many clinical applications, with substantial contributions to neurologic illnesses, oncology, and cardiovascular disease [3]. Of particular interest in this paper is quantification modeling of brain receptors with PET.

PET in dynamic mode can produce sequential images of *in vivo* distribution of a radioligand over time, thus allowing quantification of binding sites as well as the affinity of a radioligand. To extract clinically or physiologically relevant information, the PET time-activity data are commonly analyzed by applying tracer kinetic modeling approaches [4] in which a tracer kinetic model describing the tracer behavior as a function of certain biological parameters is used.

Compartmental model-based analysis forms the basis for tracer kinetic modeling in dynamic imaging [5], [6], and the output parameter or parametric image is usually the binding potential (BP) or the distribution volume (DV). These compartmental modeling approaches originate from the mathematics of pharmacokinetics, and certain reasonable assumptions are usually employed to simplify the multicompartment models and minimize the number of kinetic parameters. These approaches can be mainly classified into two categories (namely *invasive* and *noninvasive*) on the basis of whether blood sampling is required. In the invasive approaches, the tracer time-activity curve (TAC) in blood (i.e., a sequence of arterial blood samples) is used as the input function in the kinetic model [7], [9]. Although, compared with noninvasive models, invasive models have some advantages, for instance, in terms of simpler models, fewer assumptions needed, and lower computational cost, invasive measurement of the input function from arterial blood samples represents a limited, but not negligible, risk of complications including thrombosis, infection, and nerve injury [10]. Therefore, there has been increasing interest in noninvasive techniques.

Several noninvasive techniques have been proposed in the literature and can be further classified into subcategories, depending on whether a reference region is needed. Examples of noninvasive techniques requiring reference data include [11], where TAC from a region on the targeted organ was used as an input function, and [12], [13], where a simplified reference model was studied. Under conditions where no reference region is available, it is of great interest to estimate both the kinetic parameters and the input function simultaneously in a noninvasive

Manuscript received September 30, 2004; revised January 21, 2005. This work was supported in part by the National Science Foundation under Grant 0000843 and the National Institutes of Health under Grants AA11653 and AG14400. The associate editor coordinating the review of this manuscript and approving it for publication was Dr. Jan C. de Munck.

Z. J. Wang is with the Department of Electrical and Computer Engineering, University of British Columbia, Vancouver, BC, Canada (e-mail: zjanew@ece.ubc.ca).

Z. Szabo is with the Department of Radiology, Johns Hopkins University Medical Institutions, Baltimore, MD 21287 USA (e-mail: zszabo@jhmi.edu).

J. Varga is with the Department of Nuclear Medicine, Medical and Health Science Centre, University of Debrecen, Hungary (e-mail: varga@ibel.dote.hu).

P. Lei and K. J. R. Liu are with the Department of Electrical and Computer Engineering and Institute for Systems Research, University of Maryland, College Park, MD 20742 USA (e-mail: leipeng@umd.edu, kjrliu@isr.umd.edu).

Digital Object Identifier 10.1109/TSP.2005.853149

fashion. Only a few works for this purpose have been reported along this research line, including the nonlinear least square method in [15], a Monte Carlo method called simulated annealing [16], which was reported to be more insensitive to noise than the nonlinear least square method, and three blind identification schemes [17], where the authors reported that the iterative quadratic maximum likelihood (IQML) method yielded the most accurate kinetic parameter estimates. The present work plans to address PET quantification with or without knowledge of the blood input function.

In conventional compartmental modeling, the region of interest (ROI)-based approach is widely employed [8], [9], [15]–[17]. As described in [8], based on an m-compartmental model, the measured concentration of the tracer over time of the tissue within this ROI, which is referred to as the TAC of the ROI, is often well modeled as the summation of a convolution of each regional tissue component response with the total tracer concentration in plasma (i.e., the input function), where the total number of compartments is the number of components plus one. It has been shown in [6] that a two-compartment model (also referred as having one tissue component) fits some dynamic PET and SPECT studies [18], where the tissue impulse response for ROI i is modeled as

$$h^{(i)}(t) = k_I^{(i)} e^{-k_O^{(i)} t} \tag{1}$$

in which the kinetic parameters k_I and k_O represent the rate constants. Most current research on the determination of the kinetic parameters has been concerned with this simple model [14]–[17].

Despite the fact that great efforts have been taken to assess the dynamic imaging data by ROI-based compartmental modeling analysis, the ROI-based approach suffers from several problems. Briefly speaking, an important shortcoming of ROI-based approaches is that tissue response in a ROI is assumed homogeneous, and the homogeneous ROIs must be drawn in advance. However, the problem of identifying different ROIs itself remains an essential challenge, and most often, we are interested in the underlying spatial heterogeneity characterization of a region since it is essential in understanding the underlying model. For instance, some researchers have commented that ROI-based methods may not be appropriate to evaluate the kinetic process when heterogeneous areas of distribution are diagnostically important [19]. Moreover, clinical observations suggest that multiple components affect the region impulse response simultaneously. In reality, each ROI (even each image voxel) may be composed of multiple tissue components. In the case of serotonin transporter imaging, the minimal number of such components is three: One represents vascular activity, one displaceable binding to the receptor of interest (called specific binding), and one nondisplaceable binding to all other tissue components (called nonspecific binding sometimes). Limited time of imaging, limited sampling rate, and image noise in PET typically do not permit application of a more complex tissue response model.

Modeling each voxel as a separate ROI is computationally intensive or even not feasible. To address the spatial heterogeneity issue in dynamic PET data analysis, a voxel-by-voxel heterogeneity analysis of fluorodeoxyglucose (FDG) kinetics has been proposed in [20], but the procedure requires a high computational cost. The factor analysis (FA) approach has been explored for separation of kinetic components [21]. However, the resulting factors are not necessarily physiological (i.e., they maynot provide direct information about the underlying receptor binding process); in addition, the factors are not quantitative and not reproducible, which limits their diagnostic usage. We note that an interesting idea was proposed in [29], where, using the input function, spectral analysis was applied for parametric image reconstruction. In [29], a large number of β values are fixed and prechosen to provide a wide range of basis functions, which are represented by $c_p(t) \otimes \exp(-\beta_k t)$. Since β values are prechosen, the problem is formulated as a linear system, and the corresponding coefficient for each basis function can be estimated by fitting the TAC to the spectral model using the non-negative least-square (NNLS) optimization algorithm. The precision of this algorithm is limited by the number of affordable basis functions and by the success of NNLS. In this work, using statistical criteria, we propose a new approach in the voxel domain while keeping the compartmental modeling approach. Specifically, we propose to construct a likelihood-based framework for estimating the spatial/temporal patterns of tissue binding with and without the measured input function.

This paper is organized as follows. In Section II, we describe a system model in the voxel domain, representing the multiple dynamic parameters and the input function, and we then formulate the problem. In Section III, we consider the condition that the blood sampling measurements are available as the input function. A subspace-based algorithm is developed, and the validity and effectiveness of the proposed scheme is examined via the data noise impacts. In Section IV, the proposed idea is extended to the situation where no blood samples are available. A computationally efficient algorithm based on subspace analysis is developed to obtain the initial estimates, and an iterative maximum likelihood (IML) technique is then applied to improve the estimation accuracy. Simulations are put into operation to demonstrate the performance of the proposed scheme. A serial two-tissue model was studied in Section V. In Section VI, the identifiability of the proposed scheme is examined by using real PET data sets. Conclusions are drawn in Section VII.

II. System Model and Formulation

In the linear conventional compartment modeling approach, tracer characterization within a ROI leads to a set of first-order differential equations. As described in [4] and [8], solving these equations directly suggests the solution that the radioactivity in an ROI at time t can be expressed as

$$c_{\mathrm{ROI}}(t) = \sum_{j=1}^{m} k_{1j} e^{-k_{2j} t} \otimes c_p(t) \tag{2}$$

where the input function $c_p(t)$ is the total plasma concentration of a radioligand, m is the number of components, k_{1j}'s and k_{2j}'s are the weight factors and rate constants, respectively, and $\otimes$ denotes a convolution operation. As we mentioned earlier, brain regions containing receptors have at least three compartments, namely, blood pool, nonspecific binding (more precisely,

it is often referred as nondisplaceable, since this compartment can be the free compartment when nonspecific binding is negligible, or be the free plus nonspecifically bound compartment), and specific binding compartments. We focus on the two-tissue compartment model since it provides stable and reproducible parameter estimates. However, the schemes developed in this paper can be generalized further and applied to more complex models, as in (2). It is worth mentioning that tracer kinetics are often represented by a serial compartmental model in PET tracer study. As a first step, we use a parallel model here since its microparameters and macroparameters are identical, whereas the parallel model leads to a simpler way for us to estimate the underlying macroparameters by employing a voxel-domain analysis. In the case of a serial model, the macroparameters need to be transformed to obtain the microparameters, as discussed later in Section V.

More specifically, the parallel two-tissue model is illustrated in Fig. 1. As in [1], we have

$$\begin{aligned} c_f(t) &= k_{1f} a_f(t), \quad \text{with } a_f(t) = c_p(t) \otimes e^{-k_{2f}t} \\ c_s(t) &= k_{1s} a_s(t), \quad \text{with } a_s(t) = c_p(t) \otimes e^{-k_{2s}t} \end{aligned} \tag{3}$$

where the time $t \geq 0$, $k_{2f} > k_{2s} > 0$, $c_f(t)$, and $c_s(t)$ are the radioactivity in the fast turnover (reflecting the sum of all kinds of nonspecific binding) and slow turnover (resulting from specific binding) pools, respectively; k_{1f} and k_{2f} (also k_{1s} and k_{2s}) are the washin (and washout) rate constants.

We now describe the factored compartment modeling by modeling each voxel as an ROI and applying a simple method to convert temporal kinetics to spatial information. Similar to the factor analysis in [1], for voxels $i = 1, \ldots, N$ within the organ of interest (i.e., brain), by using the three-factor TACs $a_f(t)$, $a_s(t)$, and $c_p(t)$, the dynamics of each voxel i is as

$$c_m(i,t) = k_{1f}(i) a_f(t) + k_{1s}(i) a_s(t) + v_p(i) c_p(t) + \epsilon(i,t) \tag{4}$$

with $k_{1f}(i)$ and $k_{1s}(i)$ being the local permeability parameters associated with voxel i; $v_p(i)$ means the plasma volume; and $\epsilon(i,t)$ is the noise term. We now describe the discrete version of the model in (4). Letting $\mathbf{a}_f$, $\mathbf{a}_s$, and $\mathbf{c}_p$ be length-P vectors sampled uniformly every T_0 sec, we have

$$\mathbf{a}_f \triangleq \mathbf{H}(e^{-k_{2f}T_0})\mathbf{c}_p; \;\; \mathbf{a}_s \triangleq \mathbf{H}(e^{-k_{2s}T_0})\mathbf{c}_p \tag{5}$$

in which the matrix $\mathbf{H}(e^{-k_{2f}T_0})$ is a nonsymmetrical Toeplitz matrix with its first column being $[1, e^{-k_{2f}T_0}, e^{-k_{2f}2T_0}, \ldots, e^{-k_{2f}(P-1)T_0}]^T$, and T_0 should be small enough to yield an accurate result. Similarly, the nonsymmetrical Toeplitz matrix $\mathbf{H}(e^{-k_{2s}T_0})$ is defined, with the first column being $[1, e^{-k_{2s}T_0}, \ldots, e^{-k_{2s}(P-1)T_0}]^T$.

However, in practice, the PET images with short-lived radionuclides as C-11 are generally acquired with increasing time intervals to compensate for the increasing relative statistical error due to radioactive decay. Therefore, we need to address the issue of nonuniform sampling. Letting $\mathbf{t} = \{t_1, t_2, \ldots, t_n\}$ indicate the arbitrary sampling times, using the uniformly

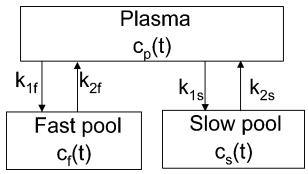

Fig. 1. PET imaging parallel two-tissue model.

sampled vectors expressed in (5), we employ the linear interpolation to represent the measurements, meaning that we have

$$\mathbf{c}_m(i) = [c_m(i,t_1), \ldots, c_m(i,t_n)]^T = \mathbf{Q}\mathbf{A}\mathbf{s}(i) + \boldsymbol{\epsilon}(i) \tag{6}$$

with $\mathbf{A} = [\mathbf{a}_f, \mathbf{a}_s, \mathbf{c}_p]$, $\mathbf{s}(i) = [k_{1f}(i), k_{1s}(i), v_p(i)]^T$, and the interpolation matrix $\mathbf{Q}$ is $n \times P$. Since simple linear interpolation is employed, each row of $\mathbf{Q}$ contains one or two nonzero elements determined by the mapping between the vector $\mathbf{t}$ and $[0, T_0, \ldots, (P-1)T_0]$. For instance, if $t_i = 2.1T_0$, then the ith row includes two nonzero elements, i.e., $Q(i,3) = 0.9$ and $Q(i,4) = 0.1$. Note that the interpolation matrix $\mathbf{Q}$ can take other forms, depending on the specific interpolation approach.

Since there are a number of sources of noise in the PET image, and several additive sources of errors tend to form a Gaussian distribution, Gaussian noise is assumed here [30]. Assume that the noise term $\epsilon(i,t)$ is both temporally and spatially white Gaussian distributed, with zero mean and variance σ^2. Therefore, for case-1, where blood samples are measured as the input function, the complete parameter set in our problem is

$$\boldsymbol{\theta} = \{k_{2f}, k_{2s}, \mathbf{s}(1), \ldots, \mathbf{s}(N), \sigma^2\}, \quad \text{for case-1} \tag{7}$$

and for case-2, where the input function is not available, we have

$$\boldsymbol{\theta} = \{k_{2f}, k_{2s}, \mathbf{c}_p, \mathbf{s}(1), \ldots, \mathbf{s}(N), \sigma^2\}, \quad \text{for case-2.} \tag{8}$$

Writing $\mathbf{X} = [\mathbf{c}_m(1), \mathbf{c}_m(2), \ldots, \mathbf{c}_m(N)]$, due to the white Gaussian noise assumption, we can derive the likelihood function $f(\mathbf{X}|\boldsymbol{\theta})$ as

$$f(\mathbf{X}|\boldsymbol{\theta}) = \prod_{i=1}^{N} (2\pi\sigma^2)^{-n/2} \exp\left(-\frac{\|\mathbf{c}_m(i) - \mathbf{Q}\mathbf{A}\mathbf{s}(i)\|^2}{2\sigma^2} \right). \tag{9}$$

We are interested in the maximum-likelihood (ML) estimate of the unknown parameters $\boldsymbol{\theta}$, due to its accuracy and robustness. Recall that the matrix $\mathbf{A}$ is fully characterized by k_{2f}, k_{2s}, and $\mathbf{c}_p$. Given $\mathbf{A}$, it is easy to show that explicit maximums with respect to σ^2 and $\mathbf{s}(i)$ are given by

$$\begin{aligned} \hat{\mathbf{s}}(i) &= (\mathbf{A}^T\mathbf{Q}^T\mathbf{Q}\mathbf{A})^{-1}\mathbf{A}^T\mathbf{Q}^T\mathbf{c}_m(i) \\ \hat{\sigma}^2 &= \frac{1}{nN}\sum_{i=1}^{N} \|\mathbf{c}_m(i) - \mathbf{Q}\mathbf{A}\hat{\mathbf{s}}(i)\|^2. \end{aligned} \tag{10}$$

In other words, with $\mathbf{A}$ being fixed, for each voxel i, the ML estimate of $\mathbf{s}(i)$ and σ^2 can be derived and substituted. Therefore, the set of parameters is reduced to $\boldsymbol{\theta}_\mathbf{s} = \{k_{2f}, k_{2s}\}$ for case-1 when measuring the input function (as measured), and

$\boldsymbol{\theta}_{\mathbf{s}} = \{k_{2f}, k_{2s}, \mathbf{c}_p\}$ for case-2. Substituting (10) into the likelihood (9), our problem is formulated in the framework of likelihood testing as obtaining the ML estimates of the parameters θ_s

$$\hat{\theta}_s = \arg\min_{\theta_s} \left\{ \sum_{i=1}^{N} \|\mathbf{c}_m(i) - \mathbf{Q}\mathbf{A}\hat{\mathbf{s}}(i)\|^2 \right\} \triangleq \arg\min_{\theta_s} L(\theta_s) \tag{11}$$

with some constraints (e.g., $k_{2f} > k_{2s} > 0$). Therefore, our goal is to simultaneously estimate these unknown parameters θ_s by minimizing the cost $L(\theta_s)$.

III. Case 1: Known Input Function

In this case, the plasma input function $c_p(t)$ is based on a sequence of arterial blood sampling measurements. The proposed scheme is described first, and then, efforts are taken to judge the validity and effectiveness of the proposed scheme by examining the impact of data noise.

A. Proposed Scheme

We propose an integrated scheme: First, a subspace-based algorithm is developed to obtain the initial estimates of the parameters. Second, with the initial guess, an optimization technique is applied to improve the estimation accuracy.

Subspace-Based Algorithm: The basic principle of subspace-based methods is to explore the spectral decomposition of a covariance matrix and use its intrinsic properties to provide a solution to an underlying estimation problem for a given observed process. The first and critical step is the separation of signal subspace and noise subspace.

In our problem, each observation vector $\mathbf{c}_m(i)$ can be regarded as the outputs of the n time-array elements at voxel position i. Based on the model in (6), the subspace spanned by the columns of $\mathbf{QA}$ is called the signal subspace, and its orthogonal subspace is termed the noise subspace. The approach of subspace-based methods is to first estimate the dominant subspace of the observations and then find the elements of $\mathbf{QA}$ that are closest to this subspace. The subspace estimation is generally achieved by performing an eigendecomposition on the estimated covariance matrix $\mathbf{R}$ of the observations. Assuming the noise and signals are uncorrelated, due to the white noise assumption, we note that the covariance matrix is expressed as

$$\begin{aligned} \mathbf{R} &= E\{\mathbf{c}_m(i)\mathbf{c}_m(i)^T\} = \mathbf{Q}\mathbf{A}\mathbf{D}_0\mathbf{A}^T\mathbf{Q}^T + \sigma^2\mathbf{I}_n \\ &= \mathbf{Q}_s\Lambda_s\mathbf{Q}_s^T + \sigma^2\mathbf{Q}_w\mathbf{Q}_w^T \\ \text{with } \mathbf{D}_0 &= E\{\mathbf{s}(i)\mathbf{s}(i)^T\} \end{aligned} \tag{12}$$

where $\mathbf{Q}_s$ and $\mathbf{Q}_w$ consist of signal and noise eigenvectors, respectively, i.e., the span of column vectors of $\mathbf{Q}_s$ defines the so-called signal subspace. Clearly, $\mathbf{D}_0$ has a full rank $M = 3$. Thus, span$(\mathbf{Q}_s)$ is orthogonal to the space span$(\mathbf{Q}_w)$.

Note that the potential signal in our problem is presented by $\mathbf{a}_s(\alpha) = \mathbf{Q}\mathbf{H}(e^{-\alpha})\mathbf{c}_p$. More specifically, the signal subspace is spanned by $\{\mathbf{Q}\mathbf{H}(e^{-\alpha})\mathbf{c}_p\}$, with $\alpha = 0$, $k_{2f}T_0$ and $k_{2s}T_0$.

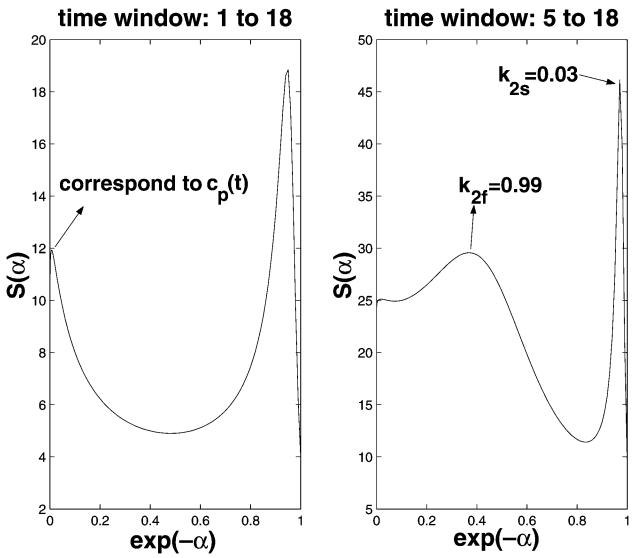

Fig. 2. Brain PET example to estimate the exponent parameters using MUSIC-like algorithm.

Therefore, to estimate the rates k_{2f} and k_{2s} and using the orthogonal property of eigendecomposition, we could develop a MUSIC-like subspace-based algorithm as

$$S(\alpha) = \frac{1}{\sum_{m=M+1}^{n} |\mathbf{q}_m^T\mathbf{a}_s(\alpha)|^2} \tag{13}$$

where $0 < e^{-\alpha} < 1$. Here, we are particularly interested in the Multiple SIgnal Classification (MUSIC) algorithm because of its wide success in many areas [24]. The tremendous interest in the subspace-based approaches is mainly due to the introduction of MUSIC. Similar to MUSIC spectrum, which exhibits peaks in frequency components, here, the peaks correspond to the exponent parameters k_{2s} and k_{2s}, e.g., by the relationship that the peak $\hat{\alpha} = k_{2f}T_0$.

Due to the heavy noise in PET data, and since the signal vectors represented in $\mathbf{QA}$ are correlated with each other, some peaks may not show up clearly within a certain time window (i.e., subarrays). Intuitively, we note that the fast-turnover component is clearer in early time images, while the slow-turnover component is demonstrated more clearly in images of the later stage. Therefore, we process the image sequences in a temporarily sliced-window manner to find all peaks, as illustrated in Fig. 2 for the later example of the brain PET study. In this example, there are a total of 18 time points. The peak demonstrating the rate k_{2s} was found when using all observations, whereas two peaks representing the rates k_{2f} and k_{2s} were noted when using observations from time point 5 to 18. In practice, different time windows will be examined to collect all possible peaks and use them to obtain the initial estimates of k_{2f} and k_{2s}.

Further Refinement: Although the above subspace-based algorithm is computationally attractive and generally accurate, it may not always yield sufficient accuracy. We need to fully exploit the underlying data model and apply parametric algorithms, such as the maximum likelihood (ML) technique, to improve the accuracy.

We can further improve the accuracy by using $\hat{k}_{2f}$ and $\hat{k}_{2s}$ obtained above as the initial estimate and applying any standard nonlinear programming schemes to obtain the ML estimates by solving the two-dimensional problem numerically

$$\hat{\theta}_s = \{\hat{k}_{2f}, \hat{k}_{2s}\} = \arg\min_{\theta_s} L(\theta_s) = \arg\min_{\theta_s} \mathrm{Tr}\{(\mathbf{I} - \mathbf{Q}\mathbf{A}(\mathbf{A}^T\mathbf{Q}^T\mathbf{Q}\mathbf{A})^{-1}\mathbf{A}^T\mathbf{Q}^T)\hat{\mathbf{R}}\} \tag{14}$$

after plugging the ML estimate of $\mathbf{s}(i)$'s in (10) into (11), with $\hat{\mathbf{R}}$ being the sample covariance matrix defined as $\hat{\mathbf{R}} = (1/N)\sum_{i=1}^{N} \mathbf{c}_m(i)\mathbf{c}_m(i)^T$, and Tr means the trace operation. Clearly, compared with the subspace-based algorithm, the price paid for the increased efficiency is that a two-dimensional search is required to obtain the ML estimates of k_{2f} and k_{2s}.

An inherited problem with numerical optimization schemes is the existence of local minima (or maxima). Therefore, obtaining a sufficiently accurate initial estimate is critical for achieving the desired global minimum. However, obtaining an appropriate initial estimate is not an easy task, and generally, convergence to the global minimum is not guaranteed in numerical optimization problems. The estimate from a subspace-based method is naturally a good choice for an initial estimate, provided that it follows the underlying signal model.

B. Examine Data Noise Impact

In the above problem formulation, certain assumptions are made to simplify the problem (e.g., the measured input function is noise-free, and there is white Gaussian noise in the voxel TACs). Ultimately, it is desirable to evaluate the validity of such assumptions and examine the performance of the proposed scheme. Errors in the proposed estimates can arise from a number of sources, such as the validity of the three-compartment model for this problem, imperfect measurements, and an imprecisely known noise model. It is beyond the scope of this paper to evaluate all these error sources. In this section, we focus on the noise factor, and efforts are taken to judge the validity and effectiveness of the proposed scheme by examining the data noise impacts. We consider different noise models and evaluate the proposed scheme by examining its effects on both the input function and the measured voxel TAC observations.

Noise is added to simulated, error-free PET TACs, which are generated as follows. First, we apply the proposed scheme to real brain receptor study, which is analyzed to get the results shown in Figs. 6 and 7, and record the estimates $\hat{\mathbf{A}}$ and $\{\hat{\mathbf{s}}(i)\}$. We then denote the original measured blood samples $\mathbf{c}_p$ as the ideal input function and denote the estimate of each voxel TAC $\hat{\mathbf{c}}_m(i) = \mathbf{Q}\hat{\mathbf{A}}\hat{\mathbf{s}}(i)$ as the ideal noise-free TAC.

In order to evaluate the proposed scheme in terms of parameter estimation of the rate constants k_{2f} and k_{2s}, we may examine various statistical criteria, such as mean, standard deviation, coefficient of variation, and bias. In this paper, as in [15] and [32], we consider the coefficient of variation (CV) and the relative bias

$$\mathrm{CV}(p) = \frac{\mathrm{SD}(\hat{p})}{\bar{p}}; \quad \mathrm{bias}(p) = \left|\frac{p - \bar{p}}{p}\right| \tag{15}$$

TABLE I
ESTIMATION PERFORMANCE OF THE RATE PARAMETERS WHEN DIFFERENT NOISE LEVELS c_{in} ARE ADDED TO THE INPUT FUNCTION. THE RESULTS ARE CALCULATED FROM 100 SIMULATION RUNS

c_{in}	$bias(k_{2f})$	$bias(k_{2s})$	$CV(k_{2f})$	$CV(k_{2s})$
0.01	0.0015	0.0033	0.0176	0.0191
0.05	0.0338	0.0299	0.0721	0.1070
0.1	0.118	0.039	0.083	0.110

in which p represents the true value of the individual parameter, SD is the standard deviation operation, and $\bar{p}$ is the empirical mean value obtained from simulations. It is clear that $\mathrm{CV}(p)$ and $\mathrm{bias}(p)$ make more sense than the simple average and standard deviation of the estimated parameter, since the latter criteria could obscure large fluctuations in the estimation. The above criteria $\mathrm{CV}(p)$ and $\mathrm{bias}(p)$ will be used to evaluate the estimation performance for each individual parameter.

We first examine the impact of a noisy input function that is simulated by adding noise terms into the ideal input function. As introduced in [31], the input noise terms are independent Gaussian variables with standard deviations

$$\sigma_{\mathrm{in}}(t_j) = c_{\mathrm{in}} \times c_p(t_j) \tag{16}$$

for $j = 1, \ldots, n$, with c_{in} being a constant defining the noise level. For each noise level, based on 100 simulations runs, we study the performance measures defined in (15). Table I shows the effects of the input noise on the kinetic parameters k_{2f} and k_{2s} at three noise levels (0.01, 0.05, and 0.1). Here, the true parameter values are $k_{2f} = 0.2808$ and $k_{2s} = 0.0027$. From this table, we can see that the resulting CVs and relative biases are reasonably small, even at noise level 10%. This observation is consistent with the observation discussed in [31] that, if the number of blood samples is sufficiently large, a moderate noise level does not affect the parameter estimation accuracy significantly.

We then examine the noise impact on voxel TAC observations that are simulated by adding noise terms into the ideal TACs $\{\hat{\mathbf{c}}_m(i)\}$. We consider two noise models for voxel TACs. The first one is consistent with the assumption in (6), where the noise terms $\{\epsilon(i,t)\}$ follow independent and identically distributed (iid) Gaussian with zero mean and variance σ^2. The second noise model is more realistic. As suggested in [30] and [31], the measurement error variance is proportional to the imaged radioactivity concentration and is inversely proportional to the scan duration; therefore, we consider the second noise model, whose noise terms $\{\epsilon(i,t)\}$ are independent Gaussian distributed with the variances described as

$$\sigma^2(i,t_j) = \mathrm{var}(\epsilon(i,t_j)) = \frac{c \times c_m(i,t_j)}{t_j - t_{j-1}} \tag{17}$$

for $j = 1, \ldots, n$, where c is a constant determining the noise level. Clearly, the second noise model indicates model-mismatch in the proposed formulation. For each noise level (i.e., represented by σ^2 in Model 1 or c in Model 2), based on 100 simulation runs, we study the performance measures discussed above. Table II shows the statistical results of estimating the parameters k_{2f} and k_{2s}. For Model 1, when the noise levels $\sigma = 50$ and 150, the corresponding signal-to-noise ratios (SNRs) are approximately 89.9 and 10, respectively. Here, the

TABLE II
ESTIMATION PERFORMANCE OF THE RATE PARAMETERS WHEN DIFFERENT NOISE LEVEL IS ADDED TO THE VOXEL TACS. THE RESULTS ARE CALCULATED FROM 100 SIMULATION RUNS

Perf. Measures vs. noise level	Model-1: σ		Model-2: c		
	50	150	1	10	30
$bias(k_{2f})$	0.0219	0.0617	0.0017	0.0038	0.0311
$CV(k_{2f})$	0.0460	0.0797	0.0182	0.0367	0.0706
$bias(k_{2s})$	0.0169	0.0345	0.0128	0.0356	0.0563
$CV(k_{2s})$	0.0860	0.1781	0.0258	0.0816	0.1312

SNR is defined as $(\sum_{j=1}^{n} \bar{c}_m(t_j)^2/n\sigma^2)$, with $\bar{c}_m(t_j)$ being the average vector of all voxel TACs. We notice that noise level $\sigma = 50$ yields very similar SNR to those observed in real PET images. From this table, we can see that the proposed scheme provides good performance under both noise models. It is encouraging to find that, although there is model mismatch in the case of Model 2, the proposed scheme still yields high estimation accuracy.

IV. CASE 2: UNKNOWN INPUT FUNCTION

In this case, $c_p(t)$ also needs to be estimated based on the voxel measurements. In other words, we propose to simultaneously estimate both the input function and the kinetic parameters. To reduce the parameter dimension of the problem, we consider a commonly adopted parametric model of the input function, as in [25], having

$$c_p(t) = (a_1 t - a_2 - a_3)e^{\lambda_1 t} + a_2 e^{\lambda_2 t} + a_3 e^{\lambda_3 t}. \quad (18)$$

This plasma TAC model has been previously validated [25] and used in simulation studies by the same authors. To remove the redundancy, we set $a_1 = 1$ and have

$$\begin{aligned}\mathbf{c}_p &= \begin{pmatrix} 0 & 1 & 1 & 1 \\ T_0 e^{\lambda_1 T_0} & e^{\lambda_1 T_0} & e^{\lambda_2 T_0} & e^{\lambda_3 T_0} \\ 2T_0 e^{2\lambda_1 T_0} & e^{2\lambda_1 T_0} & e^{2\lambda_2 T_0} & e^{2\lambda_3 T_0} \\ \vdots & \vdots & \vdots & \vdots \end{pmatrix} \\ &\quad \times \begin{pmatrix} 1 \\ -a_2 - a_3 \\ a_2 \\ a_3 \end{pmatrix} \\ &\triangleq \mathbf{B}(\lambda)\mathbf{b} \end{aligned} \quad (19)$$

in which $\lambda_1 < \lambda_2 < \lambda_3 < 0$, with $\lambda = \{\lambda_1, \lambda_2, \lambda_3\}$. Now, we note that the signal-matrix $\mathbf{A}$ is fully characterized by parameters k_{2f}, k_{2s}, λ_j's, and a_j's since

$$\mathbf{A} = [\mathbf{H}(e^{-k_{2f}T_0})\mathbf{B}(\lambda)\mathbf{b}, \mathbf{H}(e^{-k_{2s}T_0})\mathbf{B}(\lambda)\mathbf{b}, \mathbf{B}(\lambda)\mathbf{b}].$$

Now, we have the parameter set $\theta_s = \{k_{2f}, k_{2s}, \lambda_1, \lambda_2, \lambda_3, a_2, a_3\}$ in the estimation problem of interest.

A. Proposed Scheme

We develop a likelihood-based framework in the voxel domain for quantitative imaging, where radioligand kinetic parameters are estimated together with the input function. The parameters are initialized by a subspace-based algorithm and further refined by an iterative likelihood-based estimation procedure.

Subspace-Based Algorithm: Our plan is to estimate the exponent parameters k_{2f}, k_{2s}, and λ_i's by taking advantage of the special structures of the impulse response functions and the input model in (18).

For the input function as in model (18) with $a_1 = 1$, we have the Laplace transform of $c_p(t)$ as

$$\mathcal{L}\{c_p(t)\} = \frac{1}{(s-\lambda_1)^2} - \frac{a_2 + a_3}{s - \lambda_1} + \frac{a_2}{s - \lambda_2} + \frac{a_3}{s - \lambda_3}. \quad (20)$$

In addition, recall that the component impulse response function has the exponential decaying form $e^{-\alpha t}$, having $\mathcal{L}\{e^{-\alpha t}\} = (1/(s+\alpha))$. Using these properties and applying the convolution theorem, based on the system model (4), our analysis on the Laplace transform shows that the signal subspace $\mathbf{S}$ is characterized by exponential decaying signals and $te^{-\lambda_1 t}$, meaning that we have

$$\begin{aligned}\mathbf{c}_m(i) &= [\mathbf{f}_0(-k_{2f}), \mathbf{f}_0(-k_{2s}), \mathbf{f}_0(\lambda_1) \\ &\qquad \mathbf{f}_1(\lambda_1), \mathbf{f}_0(\lambda_2), \mathbf{f}_0(\lambda_3)]\mathbf{c}(i) + \epsilon(i) \\ &\triangleq \mathbf{S}\mathbf{c}(i) + \epsilon(i) \end{aligned} \quad (21)$$

where the coefficient vector $\mathbf{c}(i)$ indicates the weight of each signal component at voxel i, and $\mathbf{f}_0(\alpha)$ and $\mathbf{f}_1(\alpha)$ are the values of $e^{\alpha t}$ and $te^{\alpha t}$ sampled at $\mathbf{t}$, respectively. Now, we can write the covariance matrix as

$$\mathbf{R} = \mathbf{S}\mathbf{D}\mathbf{S}^T + \sigma^2\mathbf{I}_n, \quad \text{with } \mathbf{D} = E\{\mathbf{c}(i)\mathbf{c}(i)^T\}. \quad (22)$$

Recall that $\mathbf{R}$ can also be decomposed as in (12), where the rank of signal subspace is 3, meaning the rank of $\mathbf{D}$ in (22) is 3. Therefore, there is a rank deficiency in matrix $\mathbf{D}$. This is because the signals represented in $\mathbf{S}$ are coherent as a result of the convolution model in (4).

Therefore, before we could employ subspace-based algorithms to estimate the parameters in (21), we need to address two issues: One is rank deficiency, and the other is the nonuniform sampling time points. We first assume that the TAC measurements are uniformly sampled, meaning $\mathbf{t} = [0, T_0, 2T_0, \ldots, (n-1)T_0]$. Since, from the subspace decomposition point of view, our problem is analogous to array signal processing problems widely faced in radar, sonar, and communications [24], we can apply similar techniques to restore the rank of the source covariance matrix $\mathbf{D}$ and develop subspace-based algorithms correspondingly. For linear uniformly spaced arrays, a well-known technique to restore the rank of the signal covariance matrix is so-called *smoothing* [23], [24], in which the antenna array is split into a number of overlapping subarrays, and the covariance matrices of the subarrays are then averaged. The smoothing process introduces a random phase modulation that helps to decorrelate the source signals causing the rank deficiency. It is worth mentioning that spatial smoothing is shown [24] to work since the signal space matrix constructed of steering vectors has Vandermonde structure. In our problem, the validation of the Vandermonde structure of $\mathbf{S}$ is not so obvious due to the component $te^{-\lambda_1 t}$ in the signal space. Here, we split the uniformly sampled TACs into a number of time overlapping sub-TACs with length n_s. We show in Appendix A that $\mathbf{S}$ has Vandermonde structure as the signal components in the sub-TACs are identical up to different scalings. Thus, we present a temporal smoothing process where the covariance matrices based on sub-TACs are then averaged. Employing this temporal smoothing, we can

make $\mathbf{D}$ with a full rank $M = 6$. As long as $\mathbf{D}$ (thus $\mathbf{SDS}^T$) is of full rank, we could compute subspace-based algorithms.

Since the sampling times $\mathbf{t}$ are not uniformly spaced in practical PET images, we need to further address this nonuniform sampling issue. In radar direction-finding applications, combining the ideas of spatial smoothing and array interpolation makes it possible to restore the rank of the signal covariance matrix for arbitrary array geometries [27], [28]. The idea was tested by Monte Carlo simulations to show good performance for different test cases in [27], and its statistical performance analysis was provided in [28]. The basic idea of array interpolation is to obtain the array manifold of a *virtual* array by linear interpolation of the array manifold of the real array in the least square sense within a limited sector. Since $\mathbf{S}$ is a Vandermonde matrix when uniformly sampled, we employ similar ideas.

- We form single "virtual" uniformly spaced sampling time points $\mathbf{t}_v = [0, T_0, \ldots, (n_v - 1)T_0]$, divide the values $\beta = e^{-\alpha}$ (where $0 < e^{-\alpha} < 1$) into sectors, and design the best interpolation matrix for each sector in the least square sense. More specifically, for each sector l, we define a set of values $\mathbf{d}_l$ within the interval $\left[\beta_l^{(1)}, \beta_l^{(2)}\right]$. Compute the signal vectors associated with the set $\mathbf{d}_l$ for the given sampling time points $\mathbf{t}$ and arrange them into a matrix $\mathbf{A}_l$. Similarly, we compute the signal vectors for the interpolated $\mathbf{t}_v$ and denote the resulting matrix as $\bar{\mathbf{A}}_l$ since our basic assumption is that $\bar{\mathbf{A}}_l$ of the virtual $\mathbf{t}_v$ can be obtained through linear interpolation of $\mathbf{A}_l$ of the real $\mathbf{t}$. Thus, we estimate the interpolation matrix $\mathbf{B}_l$ such that it is the least square solution of
$$\mathbf{B}_l \mathbf{A}_l = \bar{\mathbf{A}}_l. \tag{23}$$
Remember now that the covariance matrix $\bar{\mathbf{R}}_l$ of the virtual $\mathbf{t}_v$ can be computed from the covariance matrix $\mathbf{R}_l$ of the real $\mathbf{t}$ as $\bar{\mathbf{R}}_l = \mathbf{B}_l \mathbf{R}_l \mathbf{B}_l^H$.
- We then apply the smoothing technique by splitting the TACs into a number of overlapping sub-TACs with length n_s, and the covariance matrices based on sub-TACs are averaged to obtain the smoothed covariance matrix $\bar{\mathbf{R}}^s$, as described in the Appendix. We also compute the smoothed noise covariance $\bar{\mathbf{R}}_n^s$ based on the interpolation matrix $\mathbf{B}_l$. Finally, we prewhiten the noise to obtain $\hat{\mathbf{R}} = [\bar{\mathbf{R}}_n^s]^{-1/2} \bar{\mathbf{R}}^s [\bar{\mathbf{R}}_n^s]^{-1/2H}$. We then perform the eigendecomposition on $\hat{\mathbf{R}}$ and get the signal and noise subspace.

Thus, we can restore $\mathbf{D}$ with a full rank $M = 6$. As long as $\mathbf{D}$ (thus $\mathbf{SDS}^T$) is of full rank, due to the property of eigendecomposition, we notice that the eigenvectors in $\mathbf{Q}_w$ are orthogonal to $\mathbf{S}$, meaning that
$$\mathbf{S}^T \mathbf{q}_m = 0, \quad \text{for } m = M+1, \ldots, n_s \tag{24}$$
where $\mathbf{q}_m$ are noise eigenvectors. Therefore, utilizing this orthogonality property in (24), we compute a MUSIC-like algorithm as
$$S_0(\alpha) = \frac{1}{\sum_{m=M+1}^{n_s} |\mathbf{q}_m^T \mathbf{f}_0(\alpha)|^2}$$
$$S_1(\alpha) = \frac{1}{\sum_{m=M+1}^{n_s} |\mathbf{q}_m^T \mathbf{f}_1(\alpha)|^2} \tag{25}$$
where $0 < e^{\alpha} < 1$. Similarly to the MUSIC spectrum, which exhibits peaks in the vicinity of true frequency components, here, the peaks correspond to the exponent parameters of interest. We use the constraints ($k_{2f} > k_{2s} > 0$ and $\lambda_1 < \lambda_2 < \lambda_3 < 0$) to help the mapping between the peaks and the exponent parameters. Based on the mapping, several sets of the estimates of the exponent parameters can be used as parallel initial estimates. We need to further estimate the coefficients a_2 and a_3 by minimizing the cost function, as defined in (11).

Iterative Likelihood Maximum (ILM): Since the subspace-based method is biased and may not always yield sufficient accuracy, we need to fully exploit the underlying data model and apply the ML technique to improve the accuracy.

Since any prior information (belief) should be helpful in improving the accuracy, we exploit the non-negative property of the underlying factor image coefficients (e.g., $k_{1f}(i) \geq 0$). With a fixed $\mathbf{A}$, estimating the factor coefficients $\mathbf{s}(i)$ is equivalent to solving a constrained optimization problem
$$\hat{\mathbf{s}}(i) = \arg\min_{\mathbf{s}(i)} \|\mathbf{c}_m(i) - \mathbf{QAs}(i)\|^2, \quad \text{subject to } \mathbf{s}(i) \geq 0 \tag{26}$$
via applying the Lagrange multiplier theorem. We then plug in this estimate into the cost in (11) when estimating the parameters θ_s.

We can apply a seven-dimensional search to find the ML estimates. To further reduce the computational cost of the overall ML approach, here, we propose an iterative alternative, called the iterative likelihood maximization or iterative minimization, where each iteration includes five substeps by decoupling the effects of unknown parameter sets. The main idea is to achieve multidimensional minimization (or maximization) by solving successive lower dimensional minimization (or maximization) problems iteratively. This idea has its root in the Alternate Projection (AP) technique [26]. AP is conceptually simple and appears to be a good competitor to the computationally expensive ML method. The key idea of the alternative maximization in the AP approach is to iteratively update the estimates by successively performing a maximization with respect to each single parameter while all other parameters are held fixed. In our case, employing the alternative maximization idea and considering the structure of input $\mathbf{c}_p$, we feel it is more reasonable to treat the pair (λ_2, a_2)—similarly the pair (λ_3, a_3)—as a subset of parameters and update their estimates simultaneously. Therefore, letting $\theta_s^{(k)}$ denote the estimated values of θ_s at iteration k, at iteration $(k+1)$, the update of the estimate $\theta_s^{(k+1)}$ is obtained by solving the following one- or two-dimensional minimization problems: Update the ML estimates of the parameter pair (k_{2f}, k_{2s}) under constraints while fixing all other parameters; update the ML estimates of the parameter pair (λ_2, a_2); then, update the ML estimates of the parameter pair (λ_3, a_3); then, update the ML estimates of the parameter λ_1, subject to $\lambda_1 < \lambda_2^{(k+1)}$. These substeps are iteratively applied until the convergence is achieved.

Since a minimization is performed at every substep, the value of the cost function $L(\theta_s)$ keeps decreasing with the index of the iteration k. Intuitively, the algorithm reaches the bottom of the cost function $L(\theta_s)$ along lines parallel to the axes. Thus, the

above algorithm converges to a local minimum, which depends on the initial condition. It is worth mentioning that this algorithm is easy to implement, and it is computationally attractive since we only need to solve simple one- or two-dimensional optimization problems.

B. Simulation Results for Unknown Input Function

Due to the complex nature of the dynamic imaging problem and the multiple goals of our interpretation of the dynamic imaging data, it is impossible to characterize the performance of an algorithm analytically. Hence, performance demonstrations are based on simulations. In addition, due to the lack of the existing schemes in the literature in estimating both the input function and the kinetic parameters under the system model studied here, we compare our results to the true values.

The proposed scheme should accurately estimate the three factor TACs associated with the organ (i.e., $a_f(t)$), and it should locate the organ heterogeneity characterization reasonably accurately. Let $\mathbf{y}$ and $\hat{\mathbf{y}}$ be the true and estimated factor TAC, respectively. We calculate the correlation coefficient (CC) between $\hat{\mathbf{y}}$ and $\mathbf{y}$. We also study the norm of the corresponding residuals defined as $(\hat{\mathbf{y}}-\mathbf{y})$ since it is desirable for an estimator to fit the real factor curve in a least-square sense. To make a fair comparison, we perform "centering" and "normalization" on the three factor TACs over time $\mathbf{t}$ before we calculate the above performance measures.

Considering a measure of adherence to the second objective above, we calculate the CC between the estimated factor image $\{\hat{k}_{1i}\}$ and the true one. In addition, we propose PM, which is the relative distance between the true and the estimated factor coefficients, as

$$PM_f = \frac{1}{N}\sum_{i=1}^{N}\frac{|\hat{k}_{1,f}(i)-k_{1,f}(i)|}{k_{1,f}(i)}. \tag{27}$$

The smaller PM is, the better performance in revealing the spatial heterogeneous structure.

As an example, we report simulation results for the case of unknown input function, when the images are uniformly sampled every 15 sec from 0 to 10 min. The input function $c_p(t)$ is generated from the parametric model proposed in [25]. The simulated organ phantom consists of three significantly overlapped underlying factor images, where each factor image includes a light and a darker subregion, as shown in Fig. 4. The coefficients (e.g., $\{k_{1f}(i)\}$) are randomly drawn from one of the two uniform distributions. For instance, $\{k_{1f}(i)\}$ and $\{k_{1s}(i)\}$ are from the uniform distributions $U(0.1,0.4)$ and $U(0.8,1)$. The noise level is chosen as $\sigma^2=30$.

One example of the estimated "centering" factor TACs is shown in Fig. 3, where good matches are observed. We are particularly interested in the factor images that reveal the underlying spatially heterogeneity. We study the statistical behavior of the correlation coefficient between the true and estimated factor images and the performance measure PM. Correspondingly, Table III shows their empirical means and standard deviations based on the estimate of factor images from 100 simulation runs.

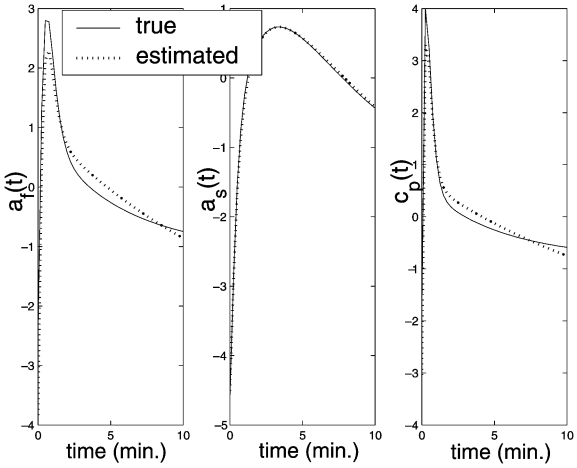

Fig. 3. True and the estimated factor TACs in simulation.

TABLE III
PERFORMANCE OF ESTIMATING THE FACTOR IMAGES, IN TERMS OF CC AND PM. IN EACH PARENTHESIS, THE FIRST NUMBER IS THE MEAN, AND THE SECOND NUMBER IS THE CORRESPONDING STANDARD DEVIATION OF THE PERFORMANCE MEASURE CC OR PM. HERE, THE NOISE LEVEL $\sigma^2=30$

factor	fast	slow	input
CC	(0.962,0.041)	(0.996,0.005)	(0.980,0.016)
PM	(0.388,0.113)	(0.110,0.079)	(0.207,0.064)

Again, we note that the proposed scheme provides good performance in estimating the underlying factor images that demonstrate the spatial heterogeneity of each component.

Since we are particularly interested in estimating the factor images, to have a better sense of the accuracy of the recovered heterogeneity indicated in Table III, one example is shown in Fig. 4. It can be seen that the proposed scheme provides high accuracy in estimating the factor images that demonstrate the spatial heterogeneity of each component.

V. MICROPARAMETERS OF THE SERIAL MODEL

So far, all our discussions focus on the parallel compartmental model described in (2). In the literature, the *in vivo* tracer kinetics are often represented by a serial compartmental model [4], [33], and measures such as binding potential (BP) and distribution volume (DV) are often calculated based on the model parameters. The serial two-tissue compartment configuration is illustrated in Fig. 5, where $c_p(t)$ represents radiotracer concentration in arterial blood, $c_f(t)$ means radioactivity in the nondisplaceable compartment, and $c_s(t)$ means radioactivity in specifically bound compartment. This system in Fig. 5 can be represented by differential equations

$$\begin{aligned}\frac{dc_s(t)}{dt} &= k_3c_f(t)-k_4c_s(t)\\ \frac{dc_f(t)}{dt} &= k_1c_p(t)-(k_2+k_3)c_f(t)+k_4c_s(t).\end{aligned} \tag{28}$$

The solution of (28) can be described as in (3). For the two-tissue compartment region, the relationships between the microparameters (i.e., k_1, k_2, k_3, and k_4) in the serial model (28) and the

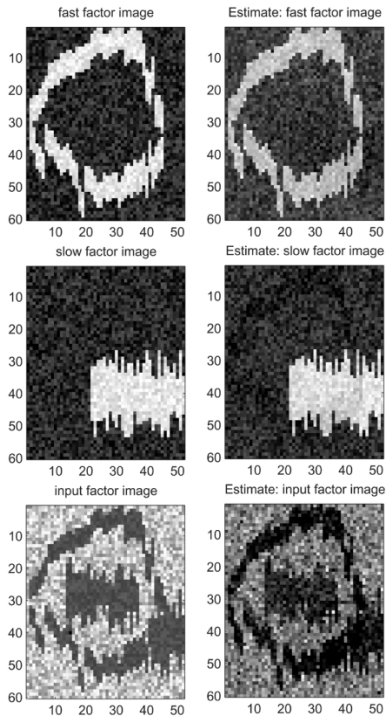

Fig. 4. Factor images in the simulated phantom of the shaped biological structures. (Left) True factor images. (Right) Estimated factor images

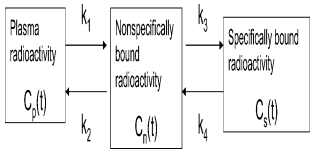

Fig. 5. PET imaging serial two-tissue compartment model.

macroparameters (i.e., k_{1f}, k_{1s}, k_{2f}, and k_{2s}) in the parallel model (3) are as follows [4], [33]:

$$\begin{aligned} k_{1s} &= \frac{k_1}{k_{2f}-k_{2s}}(k_3+k_4-k_{2s}) \\ k_{1f} &= \frac{k_1}{k_{2f}-k_{2s}}(k_{2f}-k_3-k_4) \\ k_{2s} &= \frac{1}{2}\left[k_2+k_3+k_4-\sqrt{(k_2+k_3+k_4)^2-4k_2k_4}\right] \\ k_{2f} &= \frac{1}{2}\left[k_2+k_3+k_4+\sqrt{(k_2+k_3+k_4)^2-4k_2k_4}\right]. \end{aligned} \tag{29}$$

Extending the relationships in (29) into the voxel-domain framework, based on the parameters, namely $k_{1f}(i)$, $k_{1s}(i)$, k_{2f}, and k_{2s}, estimated by the proposed scheme, we could obtain the estimates of the serial model parameters as

$$\begin{aligned} k_1(i) &= k_{1s}(i)+k_{1f}(i);\;\; k_2(i) = \frac{k_{1s}(i)k_{2s}+k_{1f}(i)k_{2f}}{k_{1s}(i)+k_{1f}(i)} \\ k_4(i) &= \frac{(k_{2s}k_{2f})}{k_2(i)} = \frac{k_{2s}k_{2f}(k_{1s}(i)+k_{1f}(i))}{k_{1s}(i)k_{2s}+k_{1f}(i)k_{2f}} \\ k_3(i) &= (k_{2s}+k_{2f})-k_2(i)-k_4(i) \\ &= \frac{k_{1s}(i)k_{1f}(i)(k_{2f}-k_{2s})^2}{(k_{1s}(i)+k_{1f}(i))(k_{1s}(i)k_{2s}+k_{1f}(i)k_{2f})}. \end{aligned}$$

Therefore, for each voxel i, we could further calculate the DVs as

$$\begin{aligned} \mathrm{DV}_{\mathrm{nonspecific}} &= \frac{k_1(i)}{k_2(i)};\;\; \mathrm{DV}_{\mathrm{specific}} = \frac{k_1(i)}{k_2(i)}\frac{k_3(i)}{k_4(i)} \\ \mathrm{BP} &= \frac{k_3(i)}{k_4(i)};\;\; \mathrm{DV}_{\mathrm{total}} = \mathrm{DV}_{\mathrm{nonspecific}} + \mathrm{DV}_{\mathrm{specific}} \\ &= \frac{k_1(i)}{k_2(i)}\left(1+\frac{k_3(i)}{k_4(i)}\right). \end{aligned} \tag{30}$$

If we are interested in calculating the DVs for a certain ROI i, the region rate $k_{1s}^{(i)}$ is now determined by the summation of all local rate $k_{1s}(j)$, where j belongs to ROI i. $k_{1f}^{(i)}$ is defined similarly. Therefore, to calculate the serial model parameters for ROI i, $k_{1s}(i)$ and $k_{1f}(i)$ are replaced by $k_{1s}^{(i)}$ and $k_{1f}^{(i)}$, respectively, in equations defined in (30).

VI. Real Datasets

We now examine the PET studies of healthy control subjects obtained after intravenous injection of C-11 labeled DASB (3-^{11}C-amino-4-(2 dimethylaminomethylphenylsulfanyl) benzonitrile), which is a radioligand used for imaging the serotonin transporter (SERT). The experimental details were the same as in [2]. In total, ten subjects were tested, and results from a typical subject are presented here. A dynamic PET study was performed with a GE Advance PET camera with an axial resolution (in full width half maximum) of 5.8 mm and an in-plane resolution of 5.4 mm. This scanner acquires 35 simultaneous 4.25-mm-thick slices. A transmission scan was first obtained with twin 10-mCi germanium-68 pin sources for 10 min for the purpose of attenuation correction of the emission scans. Eighteen serial dynamic PET images were acquired during the first 95 min after injection using the following image sequence: four 15-sec frames, three 1-min frames, three 2-min frames, three 5-min frames, three 10-min frames, and two 20-min frames. All PET scans were reconstructed using the Ramp-filtered backprojection technique in a 128×128 matrix, with a transaxial voxel size of 2×2 mm. The PET images were corrected for radionuclide decay, tissue attenuation, and injected dose of the radioligand.

For invasive determination of the input function, a radial artery line was placed by an anesthesiologist. During the PET study, arterial blood samples were withdrawn every 5–7 sec during the first 2 min and then with increasing time intervals until the end of study 95 min post injection. Exact times of blood sampling were registered. The blood samples were centrifuged, and plasma activities were counted in a gamma counter cross-calibrated with the PET scanner every day. The exact time difference between the start of the camera and the start of the gamma counter was registered for decay correction. The input function was corrected for metabolized radioligand activity. Fig. 6(a) shows the input function corrected for metabolites labeled as input (measured). For this purpose, 2-ml arterial plasma samples were obtained at 5, 15, 30, 60, and 90 min post injection. The extent of the metabolism of C-11 DASB was determined using high-performance liquid chromatography (HPLC). Missing data points of the correction function that describes the percent unmetabolized tracer were obtained by biexponential interpolation.

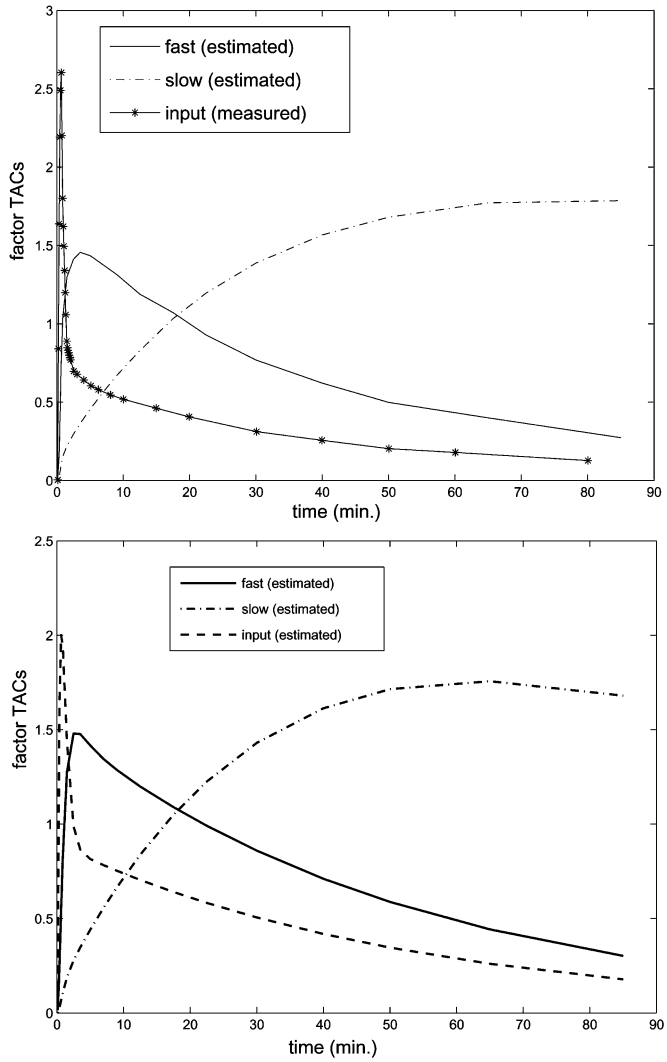

Fig. 6. Estimated factor TACs in brain PET study in the case of known (i.e., measured) (top) input function and (bottom) the case of input function estimated simultaneously with the kinetic parameters.

We first consider the case of knowing the input function by examining one subject. As a starting point, we analyze a single slice with number 15. The top of Fig. 6 shows the factor TACs estimated by the proposed scheme, where the factor curves are meaningful and follow compartmental kinetics. We further combine data from six slices, numbered 13, 15, 17, 19, 21, and 23. With all six slices, we obtain the estimates as $[k_2f, k_2s] = [0.3238, 0.0047]$ by applying the proposed scheme. Using the estimated factor TACs, we then reconstruct the factor images for all six slices simultaneously. Similarly, we combine data from slice 15 and 20, since slice 15 includes the cerebellum with predominantly fast turnover, whereas slice 20 is excellent to derive the slow factor, but it does not have the cerebellum, and it is hard to identify the fast turnover component. The reconstructed factor images are shown in Fig. 7 for slice 15 and in Fig. 8 for slice 20, where the top image represents nonspecific binding, and the bottom image appears to represent specific binding. For slice 15, as is typical in practice, the specific binding in the temporal and frontal cortex as well as in the cerebellum is lower than in the midbrain. Slice 20 shows high specific binding in the basal ganglia and midbrain, which

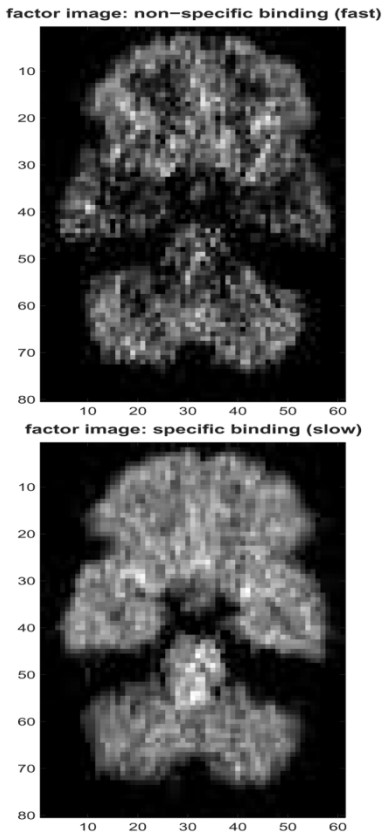

Fig. 7. Estimated factor images $\{k_{1f}(i)\}$ and $\{k_{1s}(i)\}$ of (top) nonspecific and (bottom) specific binding, respectively, from Slice 15 of the brain PET study using the measured input function and the parallel model.

is consistent with high density of the serotonin transporter in these structures.

Based on the above estimated macroparameters of the parallel model, we can obtain the estimates of microparameters of the serial model, as described in Section V. As an example, the parametric images for slice 20 are shown in Fig. 9. The top image shows the nonspecific distribution volume image of nonspecific binding obtained from the ratio of k_1/k_2. The bottom image shows the specific distribution volume image obtained as $(k_1/k_2)(k_3/k_4)$. Except some noise artifacts in the specific binding image, the two images are of reasonable quality and look similar to the images shown on Fig. 8. Of particular importance is the expected high binding in the regions on the specific binding image that correspond to higher serotonin transporter densities. On the other hand, the binding potential image (k_3/k_4) shown in the middle is very noisy, although it also shows the expected high binding in the region of basal ganglia and the midbrain.

To further evaluate the performance of the proposed scheme when the input function is available, we also report the parametric image result of the total DV for slice 20 via the popular Logan plot [34], as shown in Fig. 10. The Logan plot result is obtained by using PMT toolbox.[1] In the filtering case at the bottom of Fig. 10, a linear prefilter (with weights 4-2-1) in combination

[1]The PET-MRI Tools (PMT) software developed for processing medical images of various modalities is used for research purposes at academic institutes (See http://www.nmc.dote.hu/nmteng/pmt.htm).

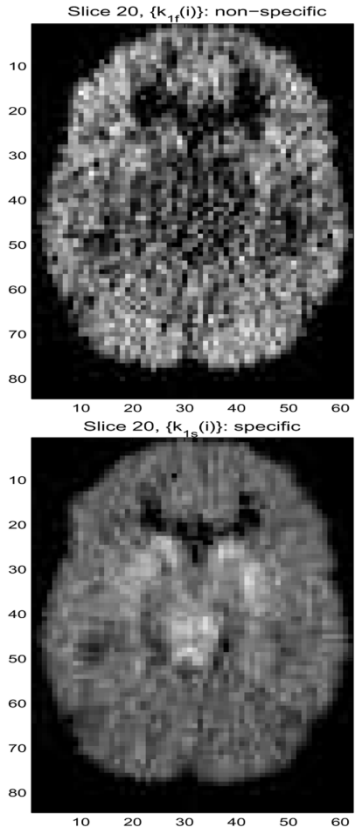

Fig. 8. Estimated factor images $\{k_{1f}(i)\}$ and $\{k_{1s}(i)\}$ of (top) nonspecific and (bottom) specific binding, respectively, from Slice 20 of the brain PET study using the measured input function and the parallel model.

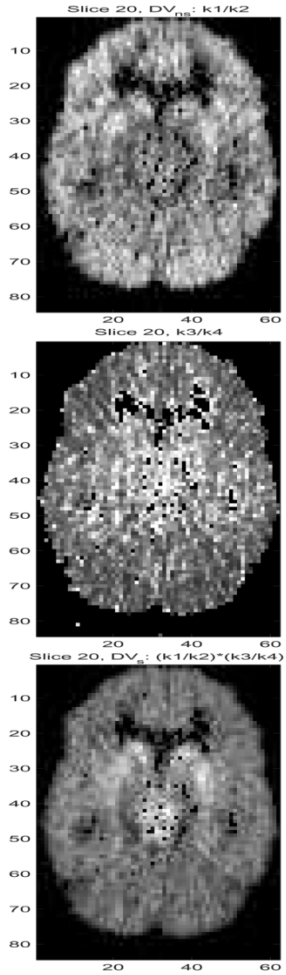

Fig. 9. Estimated voxel-by-voxel DV (distribution volume) parametric images of nonspecific and specific binding from brain PET study using the measured input function. Slice number is 20, which is identical to Fig. 8.

with a median postfilter (with mask size is 3×3) were applied. For the purpose of comparison, we plot the total DV image calculated as in (30) from the proposed scheme in Fig. 11, where in the filtering case (see the bottom of Fig. 11), a median postfilter (with mask size is 3×3) was applied. A later DASB concentration image is also provided in Fig. 12 to allow a basic feeling where the tracer is retained. We also calculated the correlation coefficient between the total DV image via the proposed scheme and that from the Logan plot. It was found that the CC is as high as 0.89 and 0.95 for the cases with and without filtering, respectively. These high CCs indicate the good match between the proposed scheme and the Logan plot. However, it is worth mentioning that the Logan plot cannot provide information about the specific DV and nonspecific DV. Since, in this paper, we want to concentrate on the effect of the proposed scheme, a no-filtering operation is considered in other figures.

Now, we further examine the case of simultaneously estimating the input function and the kinetic parameters. For comparison with the case of measuring the input function, we plot the estimated factor TACs in Fig. 6(b) and the factor images in Fig. 13 for slice 15. One can see that the pattern is comparable to the pattern derived with the measured input function. A similarly good result is obtained in slice 20. First, applying the subspace-based algorithm based on smoothing and interpolation ideas to different sectors, we obtained the estimated peak values (i.e., e^{α}) as $[0.58, 0.83, 0.92, 0.99, 0.999]$ by choosing $T_0 = 0.25$. Then, applying the iterative ML algorithm, we obtained the estimates of $\boldsymbol{\theta}_s$ as

$$\begin{aligned}\hat{\boldsymbol{\theta}}_s &= \{k_{2f}, k_{2s}, \lambda_1, \lambda_2, \lambda_3, a_2, a_3\} \\ &= [0.3342, 0.0068, -2.2093, -1.8427 \\ &\quad - 0.0300, 0.4584, 0.0775].\end{aligned}$$

The factor images for the slice with number 20 are plotted in Fig. 14. The pattern again is similar to the one obtained when the input function was available.

Similarly, we can obtain the estimates of microparameters of the serial model. First, we report the DV images in Fig. 15 for slice 20. In the upper plots, the DVs are calculated based on parameters of each voxel (upper row). Since certain smoothness is expected in DVs, for each voxel i with position $\{x_i, y_i\}$, we define a small region Ω_i characterized by $[x_i - 1, x_i + 1]$ and $[y_i - 1, y_i + 1]$. Now, for each small region Ω_i, the macroparameters are defined as $k_{1s}^{(i)} = (1/|\Omega_i|) \sum_{i \in \Omega_i} k_{1s}(i)$ and $k_{1f}^{(i)} = (1/|\Omega_i|) \sum_{i \in \Omega_i} k_{1f}(i)$. The microparameters are accordingly calculated, and the DV parametric images derived from them are shown in the lower row of Fig. 15. It is worth mentioning that more sophisticated methods of spatial regularization, such as [35], could be further explored to achieve better results.

It is worth mentioning that similar results were observed when the proposed schemes were applied to PET brain images of other control subjects.

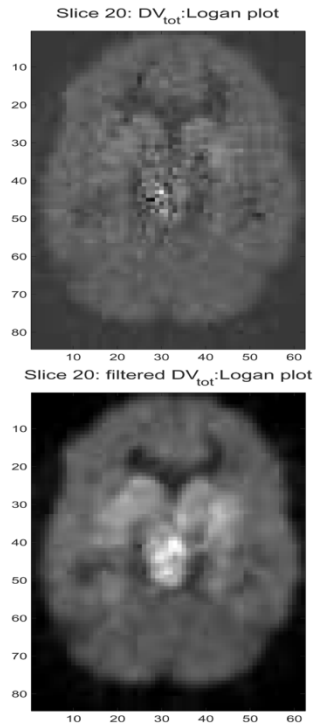

Fig. 10. Estimated voxel-by-voxel total DV parametric images from brain PET study using the Logan plot. Slice number is 20, identical to Fig. 8. On the bottom, a linear prefilter and a median postfilter were applied.

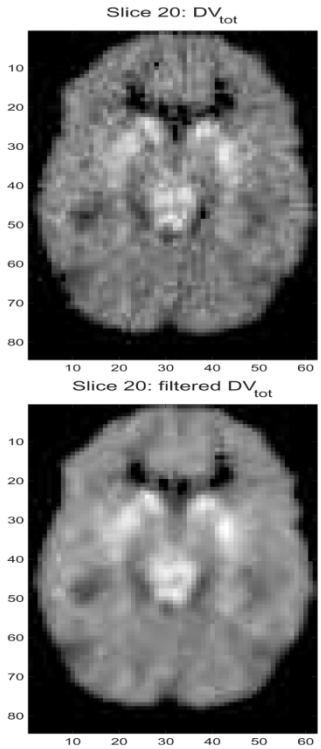

Fig. 11. Estimated voxel-by-voxel total DV parametric images from brain PET study using the measured input function. Slice number is 20, identical to Fig. 8. On the bottom, a median postfilter were applied.

VII. Conclusion

Modeling in PET allows the estimation of parameters describing receptor kinetics. In this paper, we have presented a likelihood-based framework in the voxel domain to estimate the kinetic parameters and reveal the spatial and temporal characteristics. Our contributions include the following.

- We proposed a novel approach in the voxel domain while keeping the compartmental modeling feature. Since we investigate the system model in the voxel domain, no preprocessing for identifying different ROIs on the targeted organ is required.
- We developed an efficient voxel-domain likelihood-based framework for understanding the underlying kinetics and estimating the spatial/temporal patterns of tissue binding. By taking advantage of the

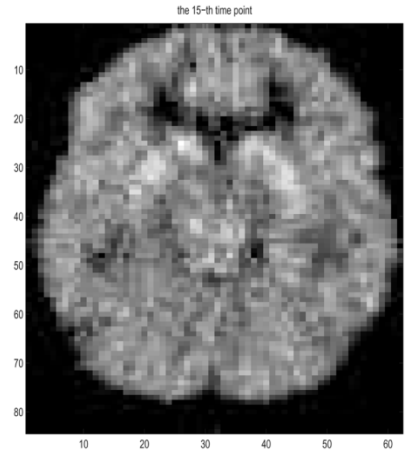

Fig. 12. Example of PET image at the 15th time point. Here, the 15th time point represents the time window from 30 to 40 min.

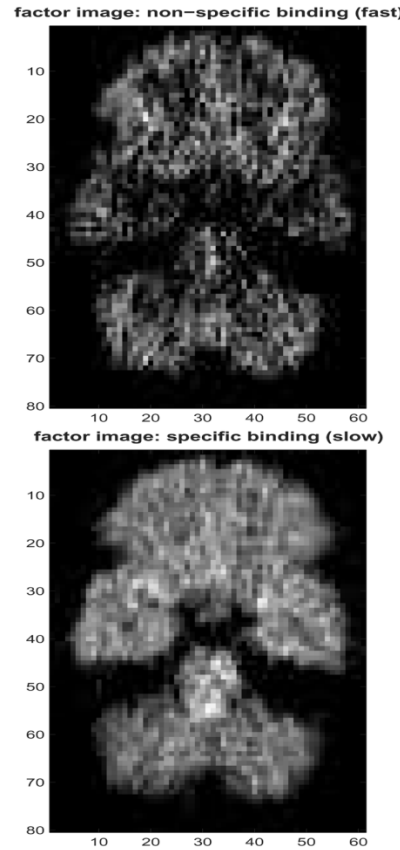

Fig. 13. Estimated factor images $\{k_{1f}(i)\}$ and $\{k_{1s}(i)\}$ of (top) nonspecific and (bottom) specific binding, respectively, from slice number 15 of the brain PET study with simultaneous estimation of the input function.

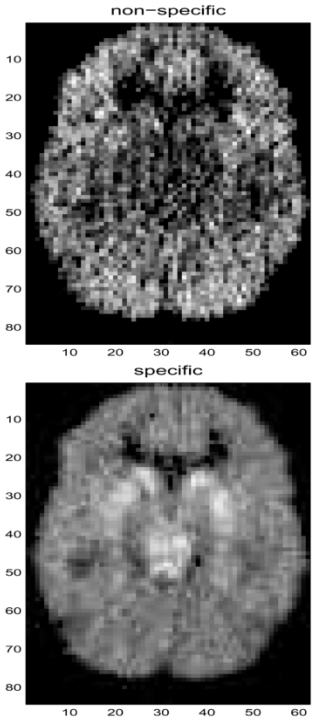

Fig. 14. Estimated factor images $\{k_{1f}(i)\}$ and $\{k_{1s}(i)\}$ of (top) nonspecific and (bottom) specific binding, respectively, from slice number 20 of the brain PET study with simultaneous estimation of the input function.

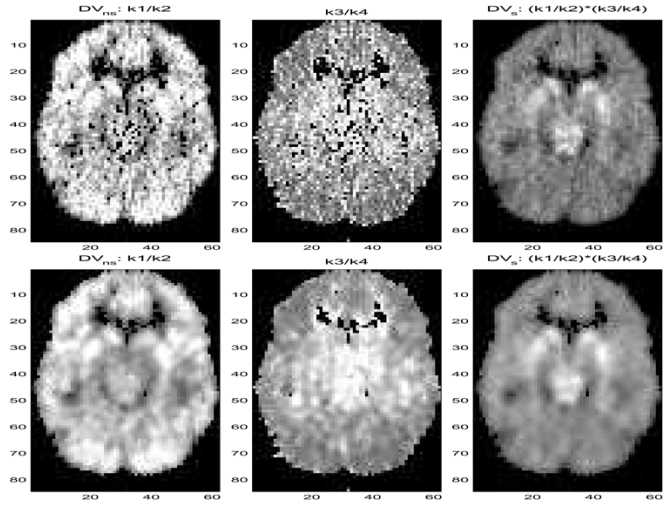

Fig. 15. Estimated distribution volume (DV) parametric images of nonspecific and specific binding from slice number 20 of the brain PET study with simultaneous estimation of the input function. In the upper row images, the DVs are calculated in each voxel; in the lower figures, the DVs are calculated for each small region to improve image smoothness.

specific signal structure, we developed subspace-based algorithms to obtain an initial estimate of the parameters. Then, an iterative likelihood maximization technique is applied to refine the estimation results.

- We derived parametric images depicting both the microparameters (i.e., k_1, k_2, k_3, and k_4) in the serial model and the macroparameters (i.e., $k_{1f}(i)$ and $k_{1s}(i)$) in the parallel model.

We studied several performance measures to examine the results of the proposed scheme in estimating the three factor TACs and in revealing the underlying spatial heterogeneous structures (e.g., the factor images and the DV images). The results illustrated that the proposed scheme is able to quantify the binding parameters and provide reliable estimations of factor TACs, and it is very promising in examining the underlying spatial heterogeneity in tissue dynamics on a voxel-by-voxel basis. Furthermore, we studied the result on brain PET data, and good performance was observed. According to the simulation and real image results, we conclude that the scheme proposed in this paper is useful for the noninvasive quantitative analysis of brain receptor dynamic PET studies.

Appendix
Temporal Smoothing Process

Here, we consider that the voxel TAC observations are uniformly sampled at the time vector $\mathbf{t} = \{0, T_0, \ldots, (n-1)T_0\}$. We split the TACs into M overlapping sub-TACs of size n_s, with time indices $\{1, \ldots, n_s\}$ forming the first sub-TAC, $\{2, \ldots, n_s + 1\}$ forming the second sub-TAC, and so on. For each voxel i, let $\mathbf{c}_{m,j}(i)$ denote the vector of the measured signals at the jth sub-TAC. Following the notation in the signal model of (21), let $\mathbf{S}_j$ denote the signal space of the jth sub-TAC and $\mathbf{D}_j$ denote a 6×6 diagonal matrix. We then have

$$\begin{aligned}\mathbf{c}_{m,j}(i) &= \mathbf{S}_j \mathbf{c}(i) + \epsilon_j(i)\\ \text{with } \mathbf{S}_j &= \mathbf{S}_1 \mathbf{E}_j\\ \mathbf{E}_j &= \text{diag}\{[T_0(j-1)+1]e^{\lambda_1(j-1)T_0}, e^{\lambda_1(j-1)T_0}\\ &\qquad e^{\lambda_2(j-1)T_0}, e^{\lambda_3(j-1)T_0}, e^{-k_{2f}(j-1)T_0}\\ &\qquad e^{-k_{2s}(j-1)T_0}\}. \end{aligned} \tag{31}$$

Therefore, the covariance matrix of the jth sub-TAC is expressed as

$$\mathbf{R}_j = \mathbf{S}_1 \mathbf{E}_j \mathbf{D} \mathbf{E}_j^T \mathbf{S}_1^T + \sigma^2 \mathbf{I}_{n_s}. \tag{32}$$

Thus, since the signal space includes both the components of $e^{\lambda_1 \mathbf{t}}$ and $\mathbf{t}e^{\lambda_1 \mathbf{t}}$, we show above that the signal components (i.e., the steering vectors) in the sub-TACs are identical up to different scalings. Correspondingly, the covariance metrics of sub-TACs can be averaged. We define the so-called temporally smoothed covariance matrix as the average of the sub-TAC covariances

$$\begin{aligned}\bar{\mathbf{R}}^s &= \frac{1}{M}\sum_{j=1}^{M} \mathbf{R}_j = \mathbf{S}_1 \left(\frac{1}{M}\sum_{j=1}^{M} \mathbf{E}_j \mathbf{D} \mathbf{E}_j^T \right) \mathbf{S}_1^T + \sigma^2 \mathbf{I}_{n_s}\\ &= \mathbf{S}_1 \bar{\mathbf{D}}_s \mathbf{S}_1^T + \sigma^2 \mathbf{I}_{n_s} \end{aligned} \tag{33}$$

where $\bar{\mathbf{D}}_s$ is the temporally smoothed covariance matrix of the signals. Since this temporal smoothing induces randomness (due to $\mathbf{E}_j$), which in turn tends to decorrelate the signals that caused the rank deficiency of $\mathbf{D}$, $\bar{\mathbf{D}}_s$ will be nonsingular when the number of sub-TACs is not less than the number of sources. In addition, we note that the covariance matrix $\bar{\mathbf{R}}^s$ has the same form as that for the noncoherent sources, with $\mathbf{S}_1$ being a subset of the full signal space. Therefore, we can successfully apply the "usual" subspace-based algorithms, such as MUSIC, after the smoothing process.

REFERENCES

[1] Y. Zhou, S.-C. Huang, T. Cloughesy, C. K. Hoh, K. Black, and M. E. Phelps, "A modeling-based factor extraction method for determining spatial heterogeneity of Ga-68 EDTA kinetics in brain tumors," *IEEE Trans. Nucl. Sci.*, vol. 44, no. 6, pp. 2522–2527, Dec. 1997.

[2] L. Kerenyi, G. Ricaurte, D. Schretlen, U. McCann, J. Varga, W. Mahews, H. Ravert, R. Dannals, J. Hilton, D. Wong, and Z. Szabo, "Positron emission tomography of striatal serotonin transporters in Parkinsons disease," *Arch. Neurol.*, vol. 60, pp. 1223–1229, 2003.

[3] S. Cherry, "Fundamentals of positron emission tomography and applications in preclinical drug development," *J. Clinical Pharmacol.*, vol. 41, pp. 482–491, 2001.

[4] M. Ichise, J. Meyer, and Y. Yonekura, "An introduction to PET and SPECT neuroreceptor quantification models," *J. Nucl. Med.*, vol. 42, no. 5, pp. 755–763, 2001.

[5] R. Gunn, R. Steve, and V. Cunningham, "Positron emission tomography compartmental models," *J. Cereb. Blood Flow Metab.*, vol. 21, no. 6, pp. 635–652, 2001.

[6] J. Vallee, H. Sostman, J. MacFall, T. Wheeler, L. Hedlund, C. Spritzer, and R. Coleman, "MRI quantitative myocardial perfusion with compartmental analysis: A rest and stress study," *Magn. Reson. Med.*, vol. 38, pp. 981–989, 1997.

[7] V. Cunningham and A. Lammertsma, "Radioligand studies in brain: Kinetic analysis of PET data," *Med. Chem. Res*, vol. 5, pp. 79–96, 1994.

[8] J. Frost *et al.*, "Multicompartmental analysis of $[^{11}C]$-carfentanil binding to opiate receptors in humans measured by positron emission tomography," *J. Cereb. Blood Flow Metab.*, vol. 9, pp. 398–409, 1989.

[9] J. Meyer and M. Ichise, "Modeling of receptor ligand data in PET and SPECT imaging: A review of major approaches," *J. Neuroimag.*, vol. 11, no. 1, pp. 30–39, 2001.

[10] J. Correia, "Editorial: A bloody future for clinical PET," *J. Nucl. Med.*, vol. 33, pp. 620–622, 1992.

[11] K. Chen, D. Bandy, E. Reiman, S. Huang, M. Lawson, D. Feng, L. Yun, and A. Palant, "Noninvasive quantification of the cerebral metabolic rate for glucose using positron emission tomography ^{18}F-fluoro-2-deoxyglucose, the patlak method, and an image-derived input function," *J. Cereb. Blood Flow Metab.*, vol. 18, pp. 716–723, 1998.

[12] A. Lammertsma and S. Hume, "Simplified reference tissue model for PET receptor studies," *Neuroimage*, vol. 4, no. 3, pp. 153–158, 1996.

[13] R. Gunn, A. Lammertsma, S. Hume, and V. Cunningham, "Parametric imaging of ligand-receptor binding in PET using a simplified reference region model," *Neuroimage*, vol. 6, no. 4, pp. 279–287, 1997.

[14] K. Wong, D. Feng, S. Meikle, and M. Fulham, "Simultaneous estimation of physiological parameters and input function—In vivo PET data," *IEEE Trans. Inf. Tech. Biomed.*, vol. 5, pp. 67–76, Mar. 2001.

[15] D. Feng, K. Wong, C. Wu, and W. Siu, "A technique for extracting physiological parameters and the required input function simultaneously from PET image measurements: Theory and simulation study," *IEEE Trans. Inf. Tech. Biomed.*, vol. 1, pp. 243–254, Dec. 1997.

[16] K. Wong, R. Meikle, D. Feng, and M. Fulham, "Estimation of input function and kinetic parameters using simulated annealing: Application in a flow model," *IEEE Trans. Nucl. Sci.*, vol. 49, no. 3, Jun. 2003.

[17] D. Riabkov and E. Bella, "Estimation of kinetic parameters without input functions: Analysis of three methods for multichannel blind identification," *IEEE Trans. Biomed. Eng.*, vol. 49, no. 11, pp. 1318–1327, Nov. 2002.

[18] E. Di Bella, R. Clackdoyle, and G. Gullberg, "Blind estimation of compartmental model parameters," *Phys. Med. Biol.*, vol. 44, pp. 765–780, 1999.

[19] G. Parker *et al.*, "Probing tumor vascularity by measurement, analysis and display of contrast agent uptake kinetics," *J. Magn. Reson. Imaging*, vol. 7, pp. 564–574, 1997.

[20] F. O'Sullivan, "Metabolic images from dynamic positron emission tomography studies," *Statist. Methods Med. Res.*, vol. 3, pp. 87–101, 1994.

[21] H. Wu *et al.*, "Factor analysis for extraction of blood time-activity curves in dynamic FDG-PET studies," *J. Nucl .Med.*, vol. 36, no. 9, pp. 1714–1722, 1995.

[22] C. Lawrence, "A Computationally Efficient Feasible Sequential Quadratic Programming Algorithm," Ph.D. dissertation, Elect. Comput. Eng. Dept., Univ. Maryland, College Park, MD, 1998.

[23] T. Shan, M. Wax, and T. Kailath, "On spatial smoothing for directions of arrival estimation of coherent signals," *IEEE Trans. Acoust., Speech, Signal Process.*, vol. ASSP-33, no. 4, pp. 806–811, Aug. 1985.

[24] H. Krim and M. Viberg, "Two decades of array signal processing research," *IEEE Signal Process. Mag.*, vol. 13, no. 4, pp. 67–93, Jul. 1996.

[25] D. Feng, S. Huang, and X. Wang, "Models for computer simulation studies of input functions for tracer kinetic modeling with positron emission tomography," *Int. J. Biomed. Comput.*, vol. 32, pp. 95–110, 1993.

[26] I. Ziskind and M. Wax, "Maximum likelihood localization of multiple source by alternate projection," *IEEE Trans. Acoust., Speech, Signal Process.*, vol. 36, no. 10, pp. 1553–1560, Oct. 1988.

[27] B. Friedlander and A. Weiss, "Direction finding using spatial smoothing with interpolated arrays," *IEEE Trans. Aerosp. Electron. Syst.*, vol. 28, no. 2, pp. 574–587, Apr. 1992.

[28] A. Weiss and B. Friedlander, "Performance analysis of spatial smoothing with interpolated arrays," *IEEE Trans. Signal Process.*, vol. 41, no. 5, pp. 1881–1892, May 1993.

[29] S. Meikle, J. Matthews, V. Cunningham, D. Bailey, L. Livieratos, T. Jones, and P. Price, "Parametric image reconstruction using spectral analysis of PET projection data," *Phys. Med. Biol.*, vol. 43, pp. 651–666, 1998.

[30] V. Oikonen, "Noise Model for PET Time-Radioactivity Curves," Turku PET Centre Modeling Rep. TPCMOD0008, Turku, Finland, 2003.

[31] K. Chen, S. Huang, and D. Yu, "The effects of measurement errors in the plasma radioactivity curve on parameter estimation in positron emission tomography," *Phys. Med. Biol.*, vol. 36, pp. 1183–1200, 1991.

[32] S. Chen, C. Ho, D. Feng, and Z. Chi, "Tracer kinetic modeling of ^{11}C-acetate applied in the liver with positron emission tomography," *IEEE Trans. Med. Imag.*, vol. 23, no. 4, pp. 426–432, Apr. 2004.

[33] H. Sasaki, I. Kanno, M. Murakami, F. Shishido, and K. Uemura, "Tomographic mapping of kinetic rate constants in the fluorodeoxyglucose model using dynamic positron emission tomography," *J Cereb. Blood Flow Metab.*, vol. 6, no. 4, pp. 447–54, 1986.

[34] J. Logan *et al.*, "Graphical analysis of reversible radioligand binding from time-activity measurements applied to [N-^{11}C-methyl]-(-)-cocaine PET studies in human subjects," *J. Cereb. Blood Flow Metab.*, vol. 10, pp. 740–747, 1990.

[35] F. Frouin, A. Cesare, Y. Bouchareb, A. Todd-Pokropek, and A. Herment, "Spatial regularization applied to factor analysis of medical image sequences (FAMIS)," *Phys. Med. Biol.*, vol. 44, no. 9, pp. 2289–2306, 1999.

Z. Jane Wang received the B.S. degree from Tsinghua University, Beijing, China, in 1996, with highest honors, and the M.S. and Ph.D. degrees from the University of Connecticut, Storrs, in 2000 and 2002, respectively, all in electrical engineering.

She is currently an assistant professor with the Electrical and Computer Engineering Department, University of British Columbia, VAncouver, BC, Canada. Previously, she was a Research Associate with the Department of Electrical and Computer Engineering, and the Institute for Systems Research, University of Maryland, College Park. Her research interests are in the broad area of statistical signal processing, information security, genomic and biomedical signal processing and statistics, and wireless communications.

Dr. Wang received the Outstanding Engineering Doctoral Student Award from the University of Connecticut.

Zsolt Szabo received the medical degree from the University of Belgrade, Belgrade, Yugoslavia. He pursued additional graduate training at Johns Hopkins before completing his residency at Hospital Barmen, Wuppertal, Germany. He was certified in nuclear medicine by the German Medical Association, then received the Ph.D. degree from the University of Dusseldorf and Nuclear Research Center, Julich, Germany.

He is attending nuclear medicine physician with the Johns Hopkins Medical Institutions, Baltimore, MD, and a leading figure in the Johns Hopkins Hospitals clinical PET service. He came to Johns Hopkins in 1989 for postgraduate training and joined the faculty in 1992. He has authored 58 articles in peer-reviewed journals and 31 chapters in medical textbooks. He is co-editor of the textbook *Principles of Nuclear Medicine* (Philadelphia, PA: Saunders, 1995) and is a reviewer for several journals in the field, including *J. Nuclear Med.*. His special research interest is in the investigation of serotonin and dopamine transporter in the brain with PET. He has also developed new methods for PET imaging of the peripheral angiotensin and endothelin receptors.

Peng Lei received the B.E. degree in biomedical engineering from Shanghai Jiao Tong University, Shanghai, China, in 1999 and the M.E. degree in electrical engineering from Institute of Acoustics, Chinese Academy of Sciences, Beijing, China, in 2002. Currently, he is pursuing the Ph.D. degree with the Bioengineering Graduate Program, University of Maryland, College Park.

József Varga received the M.S. degree in mathematics and physics from Kossuth University of Arts and Sciences, Debrecen, Hungary, in 1979. He received the Dr.Univ. degree in medical biology in 1983 and the Ph.D. degree in biology in 1996 from the University Medical School of Debrecen, where he joined the Central Nuclear Medicine Laboratory in 1979, and served as Director of Laboratory between 1990 and 1996.

Currently, he is a Senior Research Fellow with the Department of Nuclear Medicine of the reorganized University of Debrecen. He has been the Chair for the Task Group on Measuring Techniques, Hungarian Association of Nuclear Medicine, since 1995. From 200 to 2001, he spent a 12-month NSF-NATO Research Fellowship at the Johns Hopkins University, Baltimore, MD. His main research interests are medical image processing and quantitative nuclear medicine. He has been co-author of the program package "Digital Image Analyzer for Gamma Camera" (DIAG).

Dr. Varga received the István Széchenyi Professorial Fellowship for 2002–2005.

K. J. Ray Liu (F'03) received the B.S. degree from the National Taiwan University, Taipei, Taiwan, R.O.C., in 1983 and the Ph.D. degree from the University of California, Los Angeles, in 1990, both in electrical engineering.

He is Professor with the Electrical and Computer Engineering Department and Institute for Systems Research, University of Maryland, College Park. His research interests span broad aspects of signal processing algorithms and architectures; multimedia communications and signal processing; wireless communications and networking; information security; and bioinformatics, in which he has published over 300 refereed papers.

Dr. Liu is the recipient of numerous honors and awards including IEEE Signal Processing Society 2004 Distinguished Lecturer, the 1994 National Science Foundation Young Investigator Award, the IEEE Signal Processing Societys 1993 Senior Award (Best Paper Award), and the IEEE 50th Vehicular Technology Conference Best Paper Award (Amsterdam ,The Netherlands, 1999). He also received the George Corcoran Award in 1994 for outstanding contributions to electrical engineering education and the Outstanding Systems Engineering Faculty Award in 1996 in recognition of outstanding contributions in interdisciplinary research, both from the University of Maryland. Heis the Editor-in-Chief of the IEEE SIGNAL PROCESSING MAGAZINE and was the founding Editor-in-Chief of the *EURASIP Journal on Applied Signal Processing*. He has served as an Associate Editor of the IEEE TRANSACTIONS ON SIGNAL PROCESSING, a Guest Editor of special issues on Multimedia Signal Processing of the PROCEEDINGS OF THE IEEE, a Guest Editor of the special issue on Signal Processing for Wireless Communications of the IEEE JOURNAL OF SELECTED AREAS IN COMMUNICATIONS, a Guest Editor of the special issue on Multimedia Communications over Networks of the IEEE SIGNAL PROCESSING MAGAZINE, a Guest Editor of the special issue on Multimedia over Image Processing of the IEEE TRANSACTIONS ON MULTIMEDIA, and an editor of the *Journal of VLSI Signal Processing Systems*. He is on the Board of Governors and has served as Chairman of the Multimedia Signal Processing Technical Committee of the IEEE Signal Processing Society.